International Journal of Thermophysics, Vol. 28, No. 2, April 2007 (© 2007)
DOI: 10.1007/s10765-007-0190-2

Radiative Properties of Gold Surfaces with One-Dimensional Microscale Gaussian Random Roughness

Kang Fu[1] **and Pei-feng Hsu**[1,2]

The radiative properties of engineering surfaces with microscale surface textures depend on the incident wavelength, optical properties, and temperature as well as the topography of the reflective surface. In the case of slightly rough surfaces, the traditional Kirchhoff theory on rough surface scattering may be applicable. In this study, a direct numerical solution of Maxwell's equations was developed to understand scattering from weakly to very rough surfaces. The method is the finite-difference time-domain method. The problem of interest is a set of gold surfaces with Gaussian random roughness distributions. Highly accurate experimental data are available from the earlier work of Knotts and O'Donnell in 1994. Due to the negative real component of the complex dielectric constant at the infrared light source wavelengths of 1.152 and 3.392 μm, the convoluted integral was used to convert the frequency domain electrical properties to time-domain properties in order to obtain convergent solutions. The bi-directional reflectances for both normal and parallel polarizations were obtained and compared with experimental data. The predicted values and experimental results are in good agreement. The highly specular peak in the reflectivity was reproduced in the numerical simulations, and the increase of the parallel polarization bi-directional reflectance was found to be due to the effect of a variation in the optical constant from 1.152 to 3.392 μm.

KEY WORDS: bi-directional reflectance; finite-difference time-domain method; gold surface; random roughness.

[1] Department of Mechanical and Aerospace Engineering, Florida Institute of Technology, Melbourne, Florida, 32901, U.S.A.
[2] To whom correspondence should be addressed. E-mail: phsu@fit.edu

1. INTRODUCTION

Electromagnetic wave scattering by random rough surfaces presents great theoretical and experimental challenges due to the large degrees of freedom in these systems and the need to include multiple scattering effects accurately. Scattering from patterned or random roughness surfaces and coatings is of fundamental and practical interests to many disciplines, e.g., remote sensing [1], surface optics [2], thermal control [3], wafer thermal processing [4], etc. In the past three decades, considerable experimental and theoretical progress has been made in elucidating and understanding the scattering processes involved in such problems. Rapid advances in computer modeling have resulted in new approaches, for example, finite difference methods, finite element methods, and Monte Carlo simulations, in the numerical analysis of random media scattering [5]. Numerical simulations allow us to solve the Maxwell equations exactly without the limitations of analytical approximations, for example, the Kirchhoff approximation [2] and small perturbation theory [6], whose regimes of validity are often difficult to assess [7]. On the other hand, there are also challenges to improve the numerical simulations, for example, large memory and computational time requirement in multi-dimensional and complex geometry problems. Numerical methods are often more difficult to discern various mechanisms, e.g., multiple scattering, surface waves, that contribute to the scattering from random roughness surfaces.

Several theoretical treatments have been developed to understand light scattering from very rough surfaces, for example, the ray tracing method [8,9], and the integral equation method of solving Maxwell's equations [10,11]. Due to the difficulties in computing higher-order terms and in the solution convergence, perturbation series have been limited to weakly rough surfaces [6]. Geometric ray tracing is limited to roughness being larger than the incident wavelength, so the wave interference effect can be neglected [9]. The finite-difference time-domain (FDTD) method produced highly accurate solutions to understand the light scattering process of microscale random roughness in perfect electric conductors (PEC) and dielectric surfaces [12]. For metallic surfaces, the original FDTD equations have to be modified to ensure solution convergence. This requires the use of the time-domain electrical properties to revise the difference equations. The treatment is presented in this paper.

It is not easy to experimentally produce microscale random roughness surfaces that follow the Gaussian relation requirement in the surface height distribution and the height correlation function. Knotts and O'Donnell [13] used a photoresist method to produce a set of well-defined one-dimensional Gaussian roughness gold surfaces. They measured the

coherent (or specular) and incoherent (or diffuse) components of the polarized intensities scattered from the surfaces. Their experimental results are used in this study to compare with the FDTD predictions.

2. FINITE-DIFFERENCE TIME-DOMAIN METHOD

For two-dimensional (2D) geometry, the FDTD form of the transverse electric (TE) (normal polarization) set of Maxwell's equations can be written for the incident plane, i.e., the $x-y$ plane that contains E_z, H_x, and H_y, as shown below. The finite difference form of the transverse magnetic (TM) (parallel polarization) equation set can be written similarly. The details are readily available in the original paper by Yee [14] or in any numerical electromagnetic texts [15,16], and are not repeated here. In the discretized mesh of the computational domain, **E** and **H** are spatially shifted by 1/2 space increment, and the calculation of them are temporally shifted by 1/2 time increment, so that all unknown variables at any time step can be calculated based on the variables at the previous half- and full-time step status. With the second-order central difference scheme, the TE mode Maxwell's equations in two dimensions can be expressed as

$$E_z^n(i,j)=\frac{\varepsilon-\sigma\Delta t/2}{\varepsilon+\sigma\Delta t/2}E_z^{n-1}(i,j)+\frac{\Delta t}{\varepsilon+\sigma\Delta t/2}\left\{\frac{1}{\Delta x}\left[H_y^{n-1/2}(i+1/2,j)-H_y^{n-1/2}(i-1/2,j)\right]-\frac{1}{\Delta y}\left[H_x^{n-1/2}(i,j+1/2)-H_x^{n-1/2}(i,j-1/2)\right]\right\} \quad (1a)$$

$$H_x^{n+1/2}(i,j+1/2)=\frac{\mu-\sigma^*\Delta t/2}{\mu+\sigma^*\Delta t/2}H_x^{n-1/2}(i,j+1/2)-\frac{\Delta t}{(\mu+\sigma^*\Delta t/2)\Delta y}\left[E_z^n(i,j+1)-E_z^n(i,j)\right] \quad (1b)$$

$$H_y^{n+1/2}(i+1/2,j)=\frac{\mu-\sigma^*\Delta t/2}{\mu+\sigma^*\Delta t/2}H_y^{n-1/2}(i+1/2,j)+\frac{\Delta t}{(\mu+\sigma^*\Delta t/2)\Delta x}\left[E_z^n(i+1,j)-E_z^n(i,j)\right] \quad (1c)$$

where the superscript of the field components stands for the time step, the subscript represents the spatial node location, ε is the permittivity, μ is the permeability, and σ is the electrical conductivity. Note that in Eq. (1), σ and σ^* are set to zero for dielectric and non-magnetic materials. According to Yee's notation, a spatial point in a Cartesian coordinate is written as $(i,j)=(i\Delta x, j\Delta y)$. Here, Δx and Δy are the lattice space increments in the x and y coordinate directions, and i and j are integers.

If the interface of different materials is parallel to one of the coordinate axes, the continuity of tangential **E** and **H** is naturally maintained; the algorithm itself is divergence-free in the absence of electric and magnetic charge; the time-stepping algorithm is nondissipative, which means an EM wave propagating within the mesh will not decay due to the algorithm itself. These make Yee's algorithm a robust method in solving EM field issues.

The intensity of the harmonic wave is defined as a mean value of the Poynting vector and its magnitude is expressed as

$$S(x, y) = I(x, y)d\Omega = \frac{1}{T^*}\int_0^{T^*} |\mathbf{E} \times \mathbf{H}|\, dt \tag{2}$$

where I is the radiation intensity, Ω is the solid angle in the direction of the intensity, and $T^* = 2\pi/\omega$ is the time period of the wave. The bi-directional reflectance distribution function (BRDF) can be calculated in terms of the ratio of the reflected intensity over incident energy [17]:

$$\rho(\lambda, \theta_i, \phi_i, \theta_s, \phi_s) = \frac{dI(\lambda, \theta_s, \phi_s)}{I(\lambda, \theta_i, \phi_i)\cos\theta_i d\Omega_i} \tag{3}$$

where $I(\lambda, \theta_i, \phi_i)$ is for the incident beam and $I(\lambda, \theta_s, \phi_s)$ is for the reflected or scattered intensity. The denominator is the total energy of the incident light, and the numerator is the intensity of the reflected light leaving the surface in the direction (θ_s, ϕ_s).

3. RECURSIVE CONVOLUTION TREATMENT OF THE DRUDE MODEL

The Maxwell-Ampere law in Maxwell's equations is as follows:

$$\nabla \times \hat{\mathbf{H}} = \hat{\sigma}\hat{\mathbf{E}} + \hat{\varepsilon}\frac{\partial \hat{\mathbf{E}}}{\partial t} \tag{4}$$

All quantities with a^ indicate a complex number, e.g., $\hat{\varepsilon} = \varepsilon_1 - \mathrm{i}\varepsilon_2$. Assume a time harmonic incident field,

$$\hat{\mathbf{E}} = \mathbf{E}_\mathrm{o} \exp[\mathrm{i}(\omega t - \phi)] \tag{5}$$

Then, Eq. (4) becomes

$$\nabla \times \hat{\mathbf{H}} = \left(\hat{\sigma} + \mathrm{i}\omega\hat{\varepsilon}\right)\hat{\mathbf{E}} \tag{6}$$

Substituting the complex forms of $\hat{\sigma}$ and $\hat{\varepsilon}$ into Eq. (6),

$$\begin{aligned}\nabla \times \hat{\mathbf{H}} &= [(\sigma_1 + \omega\varepsilon_2) + \mathrm{i}(-\sigma_2 + \omega\varepsilon_1)]\hat{\mathbf{E}} \\ &= [\sigma_e + \mathrm{i}\omega\varepsilon_e]\hat{\mathbf{E}} \\ &= \omega\varepsilon_o\left[\left(\frac{\sigma_1}{\omega\varepsilon_o} + \frac{\varepsilon_2}{\varepsilon_o}\right) + \mathrm{i}\left(-\frac{\sigma_2}{\omega\varepsilon_o} + \frac{\varepsilon_1}{\varepsilon_o}\right)\right]\hat{\mathbf{E}} \\ &= \omega\varepsilon_o\left[2n\kappa + \mathrm{i}\left(n^2 - \kappa^2\right)\right]\hat{\mathbf{E}} \\ &= \omega\varepsilon_o\left[\varsigma'' + \mathrm{i}\varsigma'\right]\hat{\mathbf{E}}\end{aligned} \tag{7}$$

To distinguish from ε, the dielectric function or dielectric constant is expressed as $\hat{\varsigma} = \varsigma' - \mathrm{i}\varsigma''$. σ_e and ε_e are equivalent properties and used in the FDTD equations, e.g., Eq. (1) above. When $n^2 - \kappa^2 = \varsigma' = \varepsilon_e/\varepsilon_o < 0$, the FDTD code can not converge because the coefficient of the first term on the right-hand side of Eq. (1) and similar difference equations is greater than 1 and the second term is smaller than the first term. This means E_z or H field components could have non-steady or large oscillations through time-stepping. Thus, the time-stepping does not lead to convergence of the E_z field. Many metals in the wavelength of interest, say infrared, have large negative ς'. Special treatment for such property in the difference equations is needed and discussed below.

Optical properties of the dissipative media with free carriers (electron) is usually described by the Drude model [18]:

$$\hat{\varsigma}(\omega) = 1 + \frac{\omega_p^2}{\omega(\mathrm{i}\nu_\mathrm{c} - \omega)} \tag{8}$$

where ω_p is the plasma frequency and ν_c is the damping constant. With the optical constant (n, κ) data given at $\omega, \omega_\mathrm{p}$, and ν_c can be determined as well as the static permittivity at zero frequency (ε_s), the infinite frequency permittivity (ε_∞), the relaxation time (t_o), and the susceptibility (χ). Using the convolution integral, the frequency domain relation of the displacement vector and electric vector can be converted into a time-domain relation [16]. With the time-domain relation and assuming a one-dimensional case for simplicity, a new difference equation of the electric field vector component can be derived;

$$\begin{aligned}E_z^{n+1}(i) &= \frac{\varepsilon_\infty - \sigma\Delta t/2\varepsilon_o}{\varepsilon_\infty + \sigma\Delta t/2\varepsilon_o + \chi^0} E_z^n(i) + \frac{1}{\varepsilon_\infty + \sigma\Delta t/2\varepsilon_o + \chi^0}\sum_{m=0}^{n-1} E_z^{n-m}(i)\Delta\chi^m \\ &\quad + \frac{\Delta t/\varepsilon_o}{\varepsilon_\infty + \sigma\Delta t/2\varepsilon_o + \chi^0}\left[H_y^{n-1/2}(i+1/2) - H_y^{n-1/2}(i-1/2)\right]\frac{1}{\Delta x}\end{aligned} \tag{9}$$

Table I. Statistical Properties of Rough Surfaces [13]

Surface	Height standard deviation, σ (μm)	l/e Correlation width, α (μm)	Height skewness	Height kurtosis	Second derivative skewness
A	0.25	3.5	−0.02	2.97	−0.99
B	0.53	3.1	−0.08	2.99	−1.07
C	0.70	3.2	−0.05	3.01	−1.39
D	0.86	3.2	−0.29	3.12	−1.39
E	1.18	3.4	−0.29	3.12	−1.33
F	1.40	3.4	−0.27	3.12	−1.29
G	1.73	3.4	−0.19	2.90	−1.11

It should be noted that the above equation is different from the one given in Ref. 16. The difference between Eq. (9) and the counterpart equation in Ref. 16 is that the latter used an approximated value at time step $n+1$ to represent the value at time step $n+1/2$, whereas Eq. (9) is derived based on the averaged value at time steps n and $n+1$. It is easy to extend Eq. (9) to 2D or 3D geometry. In computation, Eq. (9) is further simplified to a recursive relation so the summation and the storage of the earlier time step electric field can be avoided. Details can be found in Ref. 16 and are not repeated here. As can be seen in Eq. (9), the coefficient problem in the original FDTD Eq. (1a) is eliminated.

4. RESULTS AND DISCUSSION

The surfaces used in the FDTD simulation follow the Gaussian distribution of surface height and correlation length. The experimental surface statistics used by Knotts and O'Donnell [13] are followed in the simulations and given in Table I. The precise Gaussian surface would have height skewness equal to 0 and kurtosis equal to 3 [19]. Among all surfaces, it appears surface C is the closest to Gaussian.

Besides the mesh size, the time step size, and the surface resolution, the other important FDTD simulation parameters for random rough surface scattering are the total surface length and the total number of time steps. A longer surface length will ensure precise surface statistics will be reflected in the simulations and better averages of the final results will be obtained. Sufficient time steps would also be required so that steady-state results are obtained. However, a long surface and a large number of time steps will significantly increase the computation time [12]. A compromise between solution accuracy and computational time is necessary. At an

incident wavelength $\lambda_1 = 1.152\,\mu$m and incident angle $\theta_i = 0°$, the total surface length used in the simulation is $1000 \times (\lambda_1/20)/\text{surface} \times 60\text{surfaces} = 3000\lambda_1$ and the surface resolution is equal to the mesh size. For a surface A case at $\lambda_1 = 1.152\,\mu$m, the result is the average of two $3000\lambda_1$ surfaces to reduce the oscillations in the bidirectional reflectance distribution function (BRDF) curves. The time step is $\Delta t = 0.5[(c/\Delta x)^2 + (c/\Delta y)^2]^{-1/2}$, where $\Delta x = \lambda/20$ and $\Delta y = 0.05\mu$m. Δt is adjusted so that T^* is an integer multiple of it. At this wavelength and incident angle, all parameters used in various surface calculations were the same except for the time steps: 7000 time steps for surface A, 10000 for surface B, 15000 for surfaces C and D, 18000 for surface E, 20000 for surface F, and 25000 for surface G.

At $\theta_i = 0°$ and $\lambda_2 = 3.392\,\mu$m, the total surface length used is $1000 \times (\lambda_1/20)/\text{surface} \times 120\text{surfaces} = 6000\lambda_1$. The number of same time steps were used as for $\lambda_1 = 1.152\,\mu$m calculations, except 5000 steps were used for surface A. At $\theta_i = 30°$, only surface C results are presented in this paper: at a wavelength $\lambda_1 = 1.152\,\mu$m, a surface length of $1040 \times (\lambda_1/20)/\text{surface} \times 60\text{surfaces} = 3120\lambda_1$ and 18000 time steps were used; at $\lambda_2 = 3.392\mu$m, a surface length of $1060 \times (\lambda_1/20)/\text{surface} \times 120\text{surfaces} = 6360\lambda_1$ and 18000 time steps were used. At $\theta_i = 70°$, only surface C results are presented in this paper. For both wavelengths λ_1 and λ_2, the total surface length used in the simulation is $1128 \times (\lambda_1/20)\text{surface} \times 120\ \text{surfaces} = 6768\lambda_1$ and the number of time steps are 45000.

All the calculations were carried out on a 48-node cluster. A typical run would use 30 computer nodes and took from 15 to 48 h of computational time. Weakly rough surfaces used less CPU time than did the very rough surfaces. The perfectly matched layer boundary condition [15] is applied on the top and bottom of the computational domain. The backside of the rough surface is at the bottom of the computational domain. The periodic boundary conditions were applied to the right and left sides of the computational domain. This allows the simulation of the infinite surface length via a finite size surface, which has a surface length of at least ten correlation lengths or longer.

Another problem that may arise due to insufficient surface length is the near-to-far-field (NTFF) transformation to obtain the reflectivity property [12]. To demonstrate this problem, the reflection of incident light at $\theta_i = 70°$ from surface C was calculated with the NTFF transformation to obtain the bi-directional reflectivity. A flat surface reflection toward the specular direction of $\theta_s = 70°$ is shown in Fig. 1a, which also used the NTFF transformation to obtain the far-field intensity. The Fraunhofer diffraction pattern is clearly shown near $\theta_s = 70°$. Likewise, the BRDF of the rough surface C reveals the same diffraction for both TE and TM modes (Fig. 1b). For this particular surface, the reflection of light

incident at a large angle was then obtained by using three times the surface length in the NTFF transformation to mitigate the diffraction. The improved results will be presented later.

Figure 2 shows a comparison of the FDTD simulation and measurement [13] for all surfaces except surface C. The incident angle is 0°, and the incident plane is at the $x-y$ plane. The surface roughness height is given as $y=f(x)$, and the mean height is at $y=0$. It should be noted that measured data are not available near the incident angle. Figure 2a shows the BRDF at $\lambda_1=1.152\,\mu$m. Surface A calculation used twice the number of surfaces to minimize the oscillations in the result. Although every FDTD curve except the surface A curve has some degree of oscillations, the results show that the agreement between the FDTD predictions and measured data is good. Surface G shows larger backscattering at $\theta_s=0°$ in the measured data than in the predictions. More surfaces can be used in the FDTD calculation of surface G to reduce the difference. Figure 2b shows the BRDF at $\lambda_2=3.392\,\mu$m. In this case, each surface used a $6000\lambda_1$ total surface length in the FDTD calculation. Clearly far fewer oscillations are seen in the FDTD curves. The difference between predictions and measurements in surface G is also smaller than that in Fig. 2a. It should be pointed out that the experimental surfaces are not exactly Gaussian (Table I). Therefore, some differences should be expected.

In Fig. 3, the BRDF of two different wavelengths at $\theta_i=30°$ are shown. Overall, at a moderate incident angle, the agreement between the FDTD simulation and measured data is good. However, as expected, the agreement is better at a large wavelength ($3.392\,\mu$m) than that at a smaller wavelength ($1.152\,\mu$m). In the latter case, if the longer total surface length were used, the FDTD solution oscillations near the specular reflection direction would decrease, similar to the surface A result in Fig. 2a. However, this seems to be redundant at this point. Since σ/λ is smaller at a large wavelength, the specular or coherent component is stronger at $\lambda=3.392\,\mu$m as has been shown in Fig. 2b.

Figure 4 depicts the TE and TM mode BRDF of two incident wavelengths at $\theta_i=30°$. At a smaller wavelength of $1.152\,\mu$m, there is little difference between the two modes. On the other hand, at $3.392\,\mu$m the TM mode BRDF is clearly smaller than that of the TE mode for $0°<\theta_s<50°$, i.e., angles near the specular direction. The behavior is quite different from that at large incident angles. This will be discussed next as shown in Fig. 5.

At a very large incident angle of 70°, the TE and TM mode results of both FDTD and experiment are shown in Fig. 5. The agreement between the predictions and measurements at a $3.392\,\mu$m incident wavelength is good, but somehow a larger difference for $-10°<\theta_s<40°$ is observed

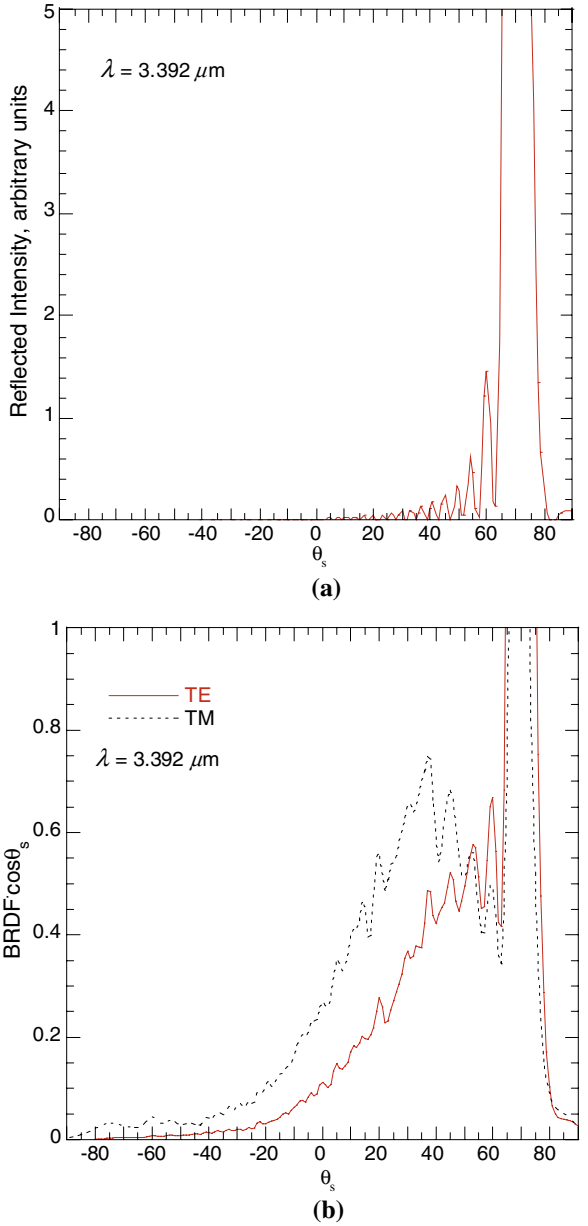

Fig. 1. Surface reflection at $\theta_i = 70°$ and with 3.392 μm light source: (a) flat gold surface with Fraunhofer diffraction and (b) scattering from surface C - the Fraunhofer diffraction pattern is apparent near the specular reflection direction.

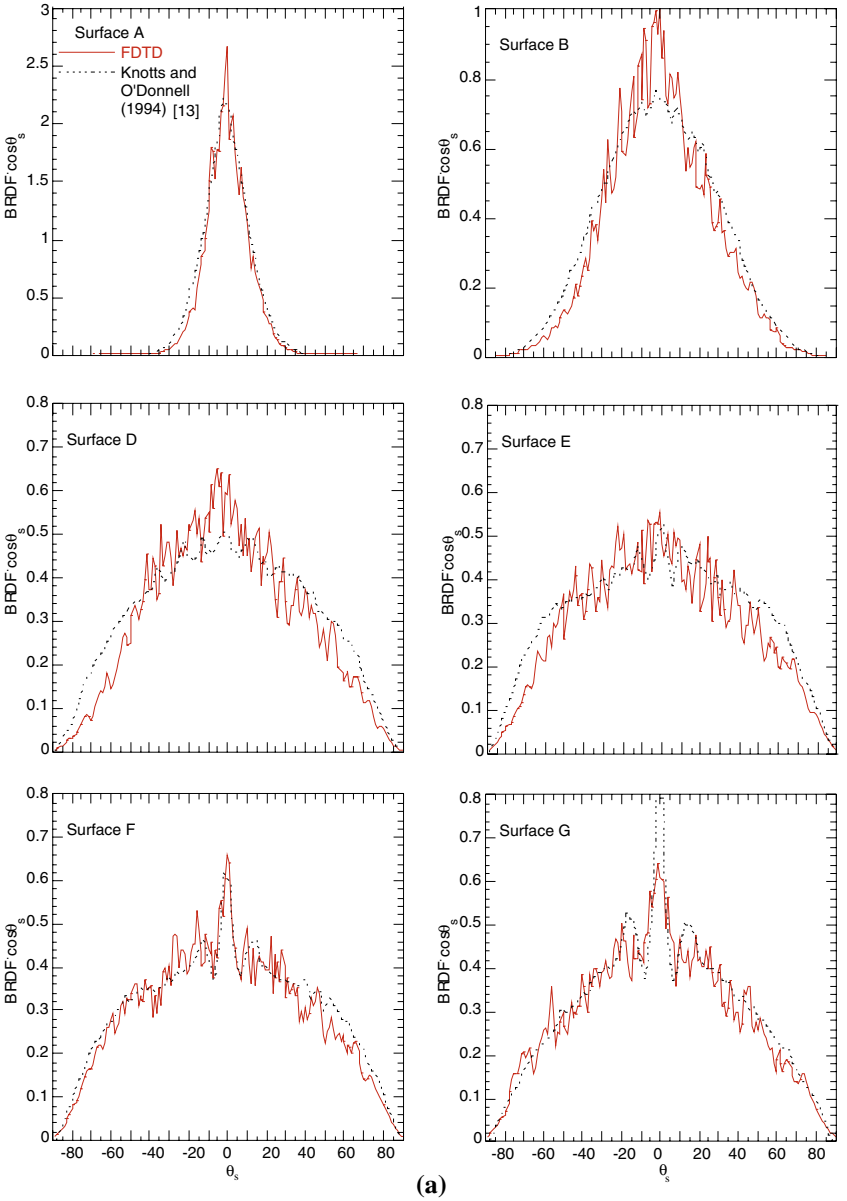

Fig. 2. (a) Angular dependence of the matrix element s_{ll} (Knotts and O'Donnell [13]) or the averaged BRDF of the TE and TM modes for surfaces A-B and D-G for $\theta_i = 0°$ and wavelength of 1.152 μm. Backscattering enhancement is seen for surfaces E-G. (b) Same as in (a) but for wavelength of 3.392 μm. Coherent components are apparent for surfaces A and B, and backscattering enhancement is seen for surfaces E-G.

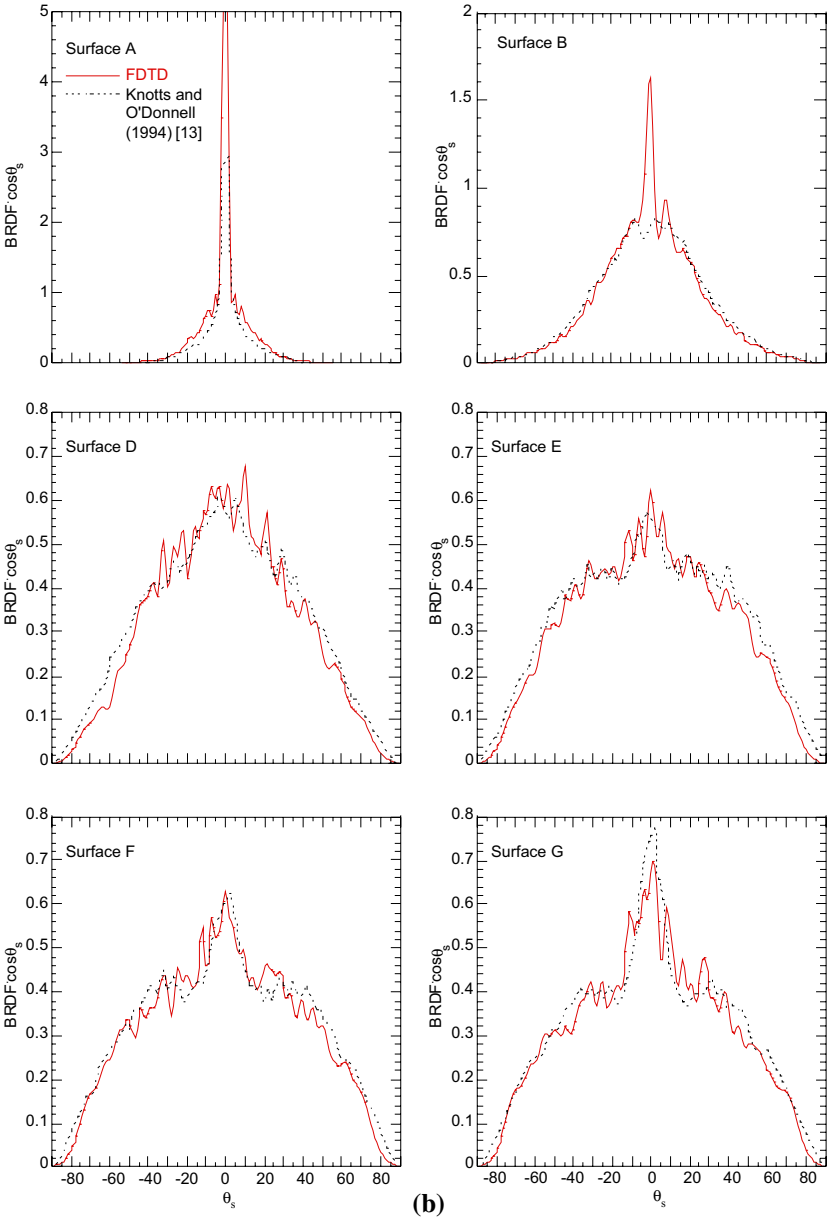

Fig. 2. Continued

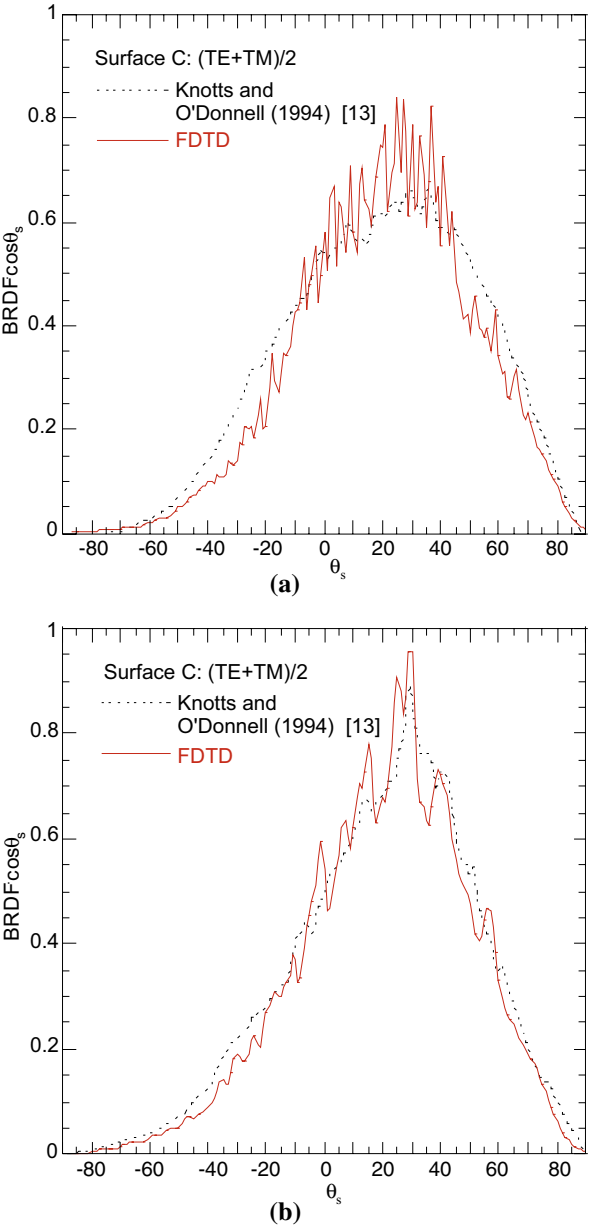

Fig. 3. Angular dependence of the BRDF for surface C for $\theta_i = 30°$: (a) incident wavelength of 1.152 μm and (b) incident wavelength of 3.392 μm. Coherent or specular components are clearly shown.

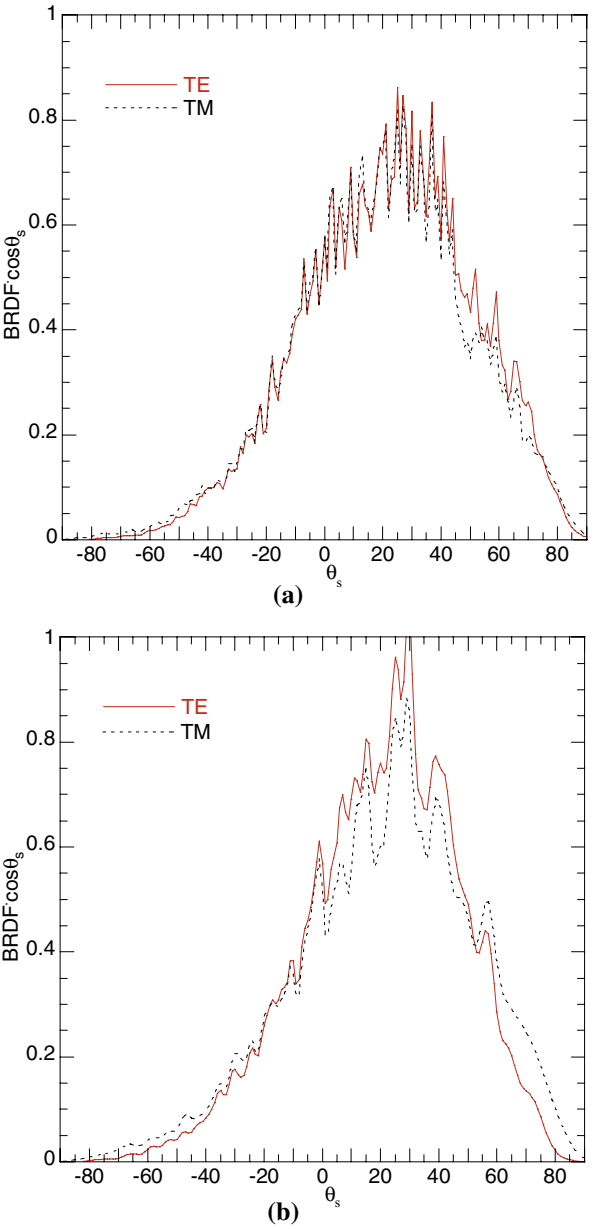

Fig. 4. Angular dependence of the TE and TM mode BRDF for surface C for $\theta_i = 30°$ for TE and TM modes based on FDTD calculations: (a) incident wavelength, 1.152 μm and (b) incident wavelength, 3.392 μm.

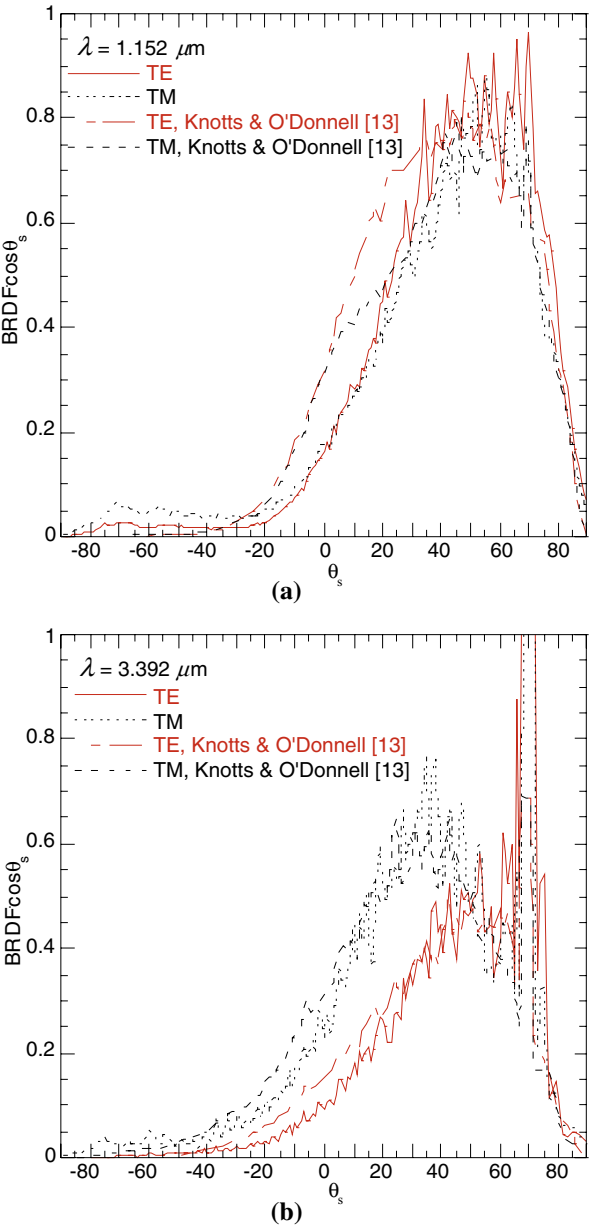

Fig. 5. Angular dependence of the TE and TM mode BRDF for surface C at $\theta_i = 70°$: (a) incident wavelength of 1.152 μm and (b) incident wavelength of 3.392 μm. Coherent components are clearly shown in both modes.

in the 1.152 μm incident wavelength results. In Fig. 5a, for $0° < \theta_s < 40°$ the experimental value for the TE mode is higher than the TM mode value. The FDTD curves confirm the difference but at a smaller level. On the other hand, at a 3.392 μm incident wavelength both experiment and FDTD show nearly the same higher TM mode than TE mode reflection. Furthermore, both results have nearly identical specular or coherent spike widths at $\theta_s = 70°$. The peak values of experimental TE and TM modes for the specular direction are not available from Knotts and O'Donnell [13]. However, the FDTD calculation shows that the TE mode value is more than twice the TM mode value at the specular direction. Over a wide range of non-specular scattering angles, the TM mode values are larger than the TE mode values at 3.392 μm and at a large incident angle as shown in Fig. 5b, which is drastically different behavior from that at a smaller wavelength of 1.152 μm (Fig. 5a) or at a smaller incident angle (Fig. 4b).

Clearly, the optical constant variation over the range from 1.152 to 3.392 μm causes the switchover of TE and TM mode values at non-specular directions. To examine its effect, the optical constant n and κ values [20] and the corresponding time domain Drude model parameters are shown in Fig. 6. The optical constants in Ref. 20 show two different values at several wavelengths but only the lower values, which are more consistent with the overall trend in the wavelength range shown, were used in the Drude model parameters of ω_p and ν_c. It is apparent that there is a sudden drop in ω_p and sudden rise in ν_c. near 1.24 μm. The change in the Drude parameters causes the switchover of the TE and TM mode values in the non-specular directions. This is shown in the calculated BRDF variation over four different wavelengths in Fig. 7. As the wavelength increases from 1.152 to 1.24 μm, the TE and TM mode values are almost identical, except at and near the specular directions. Beyond 1.24 μm, the TM mode values start to increase over the TE mode values at the non-specular directions. To understand the actual physical mechanism that causes the TE/TM mode switchover, for example, the surface plasmon polariton wave coupling [10, 11], further study is needed. This is beyond the scope of the current work and will be considered in the future.

5. CONCLUSION

A comparison with a set of highly accurate experimental data demonstrates that the finite-difference time-domain method provides validated simulation capability to predict metallic surface radiative properties at various wavelengths and surface roughnesses. A special treatment of the frequency domain electrical properties is needed to ensure convergence of the

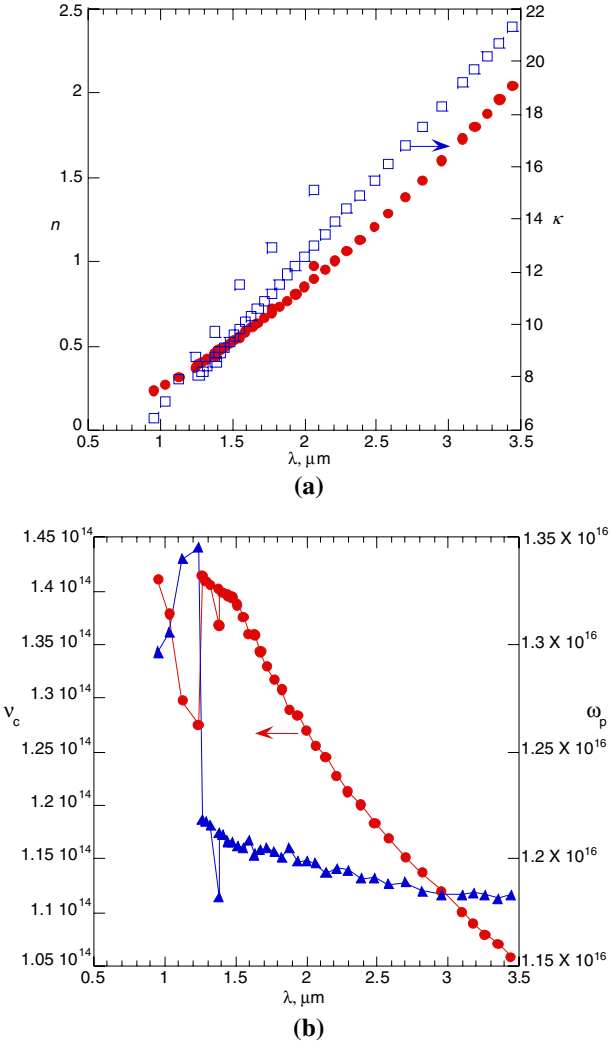

Fig. 6. Wavelength dependence of (a) optical constant and (b) time-domain Drude parameters.

numerical scheme. The numerical solutions show good agreement with the reflectivity measured from a set of microscale random roughness Gaussian gold surfaces. The numerical method also provides a new way to understand the increase of the TM mode or parallel polarization reflectivity at the non-specular directions when the incident wavelength increases

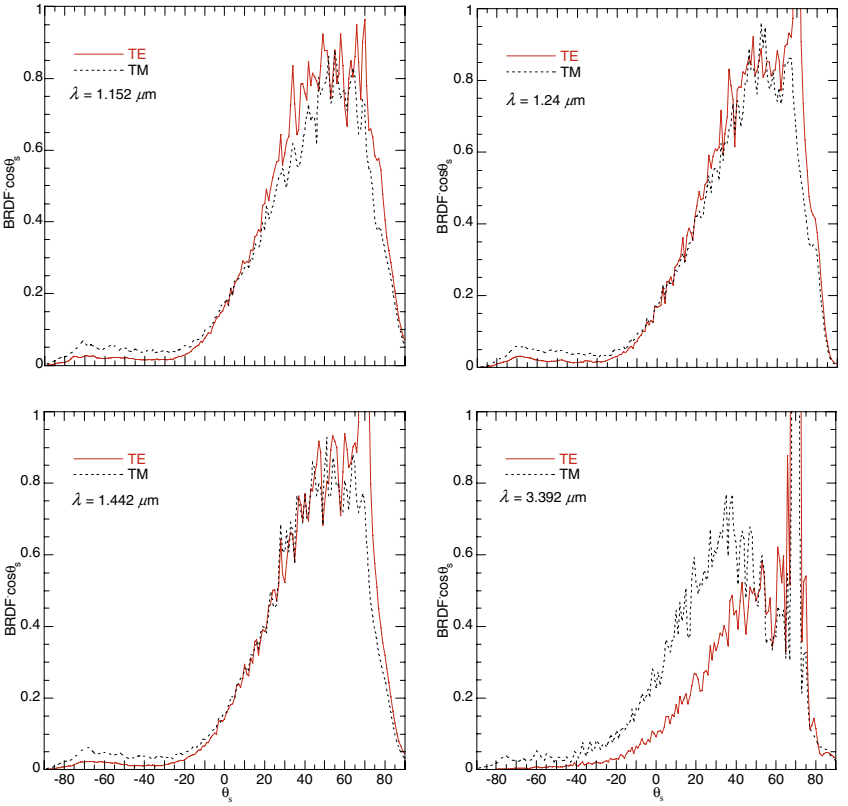

Fig. 7. Angular dependence of the TE and TM mode BRDF for surface C at $\theta_i = 70°$ and incident wavelength variation from 1.152 to 3.392 μm.

from 1.152 to 3.392 μm. The switchover of the TE and TM modes may also be caused by the reduced roughness height to wavelength ratio and the increased diffraction at longer wavelength. Further study is needed to clarify.

ACKNOWLEDGMENTS

The work is supported by a grant from the National Science Foundation, Grant No. CTS-0331153. The helpful discussions with Prof. Zhuomin Zhang of Georgia Institute of Technology on the experiment data and Prof. Xianfan Xu of Purdue University on the dielectric function treatment are much appreciated.

REFERENCES

1. T.-K. Chan, Y. Kuga, and A. Ishimaru, *IEEE Trans. Geo. Remote Sensing* **34**:673 (1996).
2. P. Beckmann and A. Spizzichino, *The Scattering of Electromagnetic Waves from Rough Surfaces*, (Artech House, Norwood, Massachusetts, 1987), Chap. 5.
3. B. L. Drolen, *AIAA J. Thermophys. Heat Transfer* 6:672 (1992).
4. J. P. Hebb, K. F. Jensen, and J. Thomas, *IEEE Trans. Semicond. Manuf.* 11:607 (1998).
5. L. Tsang, J. A. Kong, K.-H. Ding, and C. O. Ao, *Scattering of Electromagnetic Waves* – Vol. II, *Numerical Simulations* (Wiley, New York, 2000).
6. E. I. Chaikina, A. G. Navarrete, E. R. Mendez, A. Martinez, and A. A. Maradudin, *Appl. Opt*. **37**:1110 (1998).
7. L. Tsang, J. A. Kong, and K.-H. Ding, *Scattering of Electromagnetic Waves* – Vol. I, *Theories and Applications* (Wiley, New York, 2000).
8. K. Tang, P. A. Kawka, and R. O. Buckius, *AIAA J. Thermophys. Heat Transfer* **13**:169 (1999).
9. A. A. Maradudin, T. Michel, A. R. McGurn, and E. R. Mendez, *Ann. Phys.* **203**:255 (1990).
10. A. R. McGurn, A. A. Maradudin, and V. Celli, *Phys. Rev.* **B31**:4866 (1985).
11. H. J. Lee, Q. Z. Zhu, Y. B. Chen, and Z. M. Zhang, Proc. 38th *AIAA Thermophys. Conf.*, Toronto, Canada (2005).
12. K. Fu and P.-f. Hsu, *ASME J. Heat Transfer* **129**:71 (2007).
13. M. E. Knotts and K. A. O'Donnell, *J. Opt. Soc. Am.* **A11**:697 (1994).
14. K. S. Yee, *IEEE Trans. Antenn. Propagat.* **14**:302 (1966).
15. A. Taflove and S. C. Hagness, *Computational Electrodynamics: The Finite-Difference Time-Domain Method*, 3rd Ed. (Artech House, Boston, Massachusetts, 2005).
16. K. S. Kunz and R. J. Luebbers, *The Finite Difference Time Domain Method for Electromagnetics* (CRC Press, Boca Raton, Florida, 1993).
17. H. J. Lee, Y. B. Chen, and Z. M. Zhang, *Int. J. Heat Mass Transfer* **49**:4482 (2006).
18. C. F. Bohren and D. R. Huffman, *Absorption and Scattering of Light by Small Particles* (John Wiley & Sons, New York, 1983).
19. Y. Zhao, G.-C. Wang, and T.-M. Lu, *Characterization of Amorphous and Crystalline Rough Surface: Principles and Applications* (Academic Press, San Diego, California, 2001).
20. E. D. Palik, *Handbook of Optical Constants of Solids* (Academic Press, Orlando, Florida, 1985).